Journal of Materials Chemistry C

Water-soluble CaO sacrificial layer heteroepitaxially grown on yttria-stabilized zirconia substrate for large ferroelectric BaTiO3 sheets

Journal:	*Journal of Materials Chemistry C*
Manuscript ID	TC-ART-10-2024-004585.R1
Article Type:	Paper
Date Submitted by the Author:	16-Dec-2024
Complete List of Authors:	Zhou, Weikun; Hokkaido University Gong, Lizhikun; Hokkaido University Mitsuya, Ren; Hokkaido University Chen, Diwen; Hokkaido University Ohta, Hiromichi; Hokkaido University, Research Institute for Electronic Science; Hokkaido University Katayama, Tsukasa; Hokkaido University, research institute for electronic science

Water-soluble CaO sacrificial layer heteroepitaxially grown on yttria-stabilized zirconia substrate for large ferroelectric $BaTiO_3$ sheets

Weikun Zhou[1], Lizhikun Gong[2], Ren Mitsuya[1], Diwen Chen[1], Hiromichi Ohta[3] and Tsukasa Katayama[3,4]*

[1]Graduate School of Information Science and Technology, Hokkaido University, N14W9, Kita, Sapporo 060-0814, Japan

[2]Key Laboratory of Artificial Micro- and Nano-structures of Ministry of Education and School of Physics and Technology, Wuhan University, Wuhan, China

[3]Research Institute for Electronic Science, Hokkaido University, N20W10, Kita, Sapporo 001-0020, Japan

[4]JST-PRESTO, Kawaguchi, Saitama 332-0012, Japan

*Corresponding author: katayama@es.hokudai.ac.jp

Abstract

Ferroelectric perovskite oxide sheets with a high orientation and crystallinity are suitable for various applications. A promising method for their synthesis involves the combination of epitaxial growth with sacrificial layers that can be dissolved in solvents. However, the practical applications of these sacrificial layers are limited. They are typically grown on substrates such as $SrTiO_3$ single crystals, which have not yet been scaled up for large-area applications. In addition, during the lift-off process, a high density of cracks is often formed in the ferroelectric sheets. To address these issues, we used a CaO sacrificial layer in this study. We deposited a ferroelectric $BaTiO_3$ epitaxial layer on the CaO sacrificial layer, which was epitaxially grown on a [110]-oriented yttria-stabilized zirconia (YSZ) substrate, together with a protective Al_2O_3 glass layer. After dissolving the CaO layer in pure water, we successfully obtained a crack-free freestanding $BaTiO_3$ sheet with a lateral size of 5 mm × 2 mm. The resulting $BaTiO_3$ sheet exhibited room-temperature ferroelectricity and piezoelectric properties with a large d_{33} value of 270 pm/V owing to the release of strain from the substrate. In addition, the YSZ substrate could be reused. Our study expands the range of water-soluble sacrificial layers and substrates for obtaining large ferroelectric and piezoelectric oxide epitaxial sheets.

1. Introduction

Ferroelectric oxides with perovskite structures have garnered significant attention because of their high permittivity, high piezoelectricity, and excellent electro-optic properties. These functionalities enable their wide applications in electronic devices such as multilayer ceramic capacitors, piezoelectric microelectromechanical systems, and optical communication technologies [1–6]. In ferroelectric crystals, polarization occurs in only one direction, leading to a high demand for ferroelectric materials with high orientation and crystallinity to enhance their functionality. A promising approach is the epitaxial growth of these materials using single-crystal substrates.

Recently, the detachment of highly oriented and crystalline ferroelectric oxide films from their substrates and their subsequent transfer to Si-based electronic devices or flexible materials have garnered increasing interest, leading to an expansion of their applications [7–16]. In the chemical lift-off and transfer processes of ferroelectric oxide thin films, the ferroelectric layer is epitaxially grown on a sacrificial layer deposited on a single-crystal substrate. When the as-prepared thin film is immersed in a solvent, the sacrificial layer dissolves, allowing the ferroelectric film to separate from the substrate.

One of the most commonly used sacrificial layers is $Sr_3Al_2O_6$, which dissolves in water and causes minimal damage to the ferroelectric layer [7]. In addition, the lattice constant of $Sr_3Al_2O_6$ (cubic structure with $a/4$ = 0.3961 nm) is close to that of the ferroelectric layers with a perovskite structure, enabling the growth of highly crystalline ferroelectric layers. The lattice constant of $Sr_3Al_2O_6$ can be tuned by doping with Ca or Ba [17,18]. Other sacrificial layers have also been used to synthesize thin oxide sheets. Sacrificial layers with perovskite-type structures, such as $La_{0.7}Sr_{0.3}MnO_3$, $SrVO_3$, $SrCoO_{2.5}$, $YBa_2Cu_3O_7$, and $SrRuO_3$, can be dissolved in acids [19–23]. Moreover, sacrificial layers with NaCl-type structures, such as BaO and $Sr_{1-x}Ca_xO$ ($0 \leq x \leq 1$), can be dissolved in pure water [24,25]. Highly oriented ferroelectric oxide sheets with perovskite structures, such as $BiFeO_3$, $BaTiO_3$, and lead zirconate titanate (PZT), have been successfully obtained via the lift-off method using these sacrificial layers [10,19,26].

However, the practical applications of these sacrificial layers are limited. For example, these

layers are typically grown on substrates such as $SrTiO_3$ (STO) single crystals, which are not yet scalable to larger areas, rendering industrial use difficult. Furthermore, a high density of cracks is often formed during the lift-off process, thereby complicating the fabrication of large-area freestanding sheets. In this study, we demonstrate the use of an easily obtainable sacrificial layer, CaO, for fabricating a ferroelectric $BaTiO_3$ (BTO) epitaxial film on a yttria-stabilized zirconia (YSZ) substrate. Compared to STO, YSZ can form larger single crystals, and using YSZ as a substrate is also more cost-effective [27,28]. After dissolving the CaO layer in pure water, a crack-free freestanding BTO sheet with a lateral size of 5 mm × 2 mm was successfully obtained. The resulting BTO sheet exhibited both ferroelectric and piezoelectric properties. In addition, the YSZ substrate could be reused after ultrasonic cleaning in pure water, thereby demonstrating the practical applicability of the CaO sacrificial layer.

2. Experiment

The as-grown film was grown on a [110]-oriented YSZ [YSZ(110)] substrate using the pulsed laser deposition (PLD) technique. The film consisted of four layers: CaO, BTO, indium-tin oxide (ITO), and Al_2O_3 glass. The substrate temperature and oxygen partial pressure were maintained at 1×10^{-5} Torr and 500 °C for the CaO layer, 6×10^{-3} Torr and 790 ℃ for the BTO layer, 3×10^{-2} Torr and 200 °C for the ITO layer, and 1×10^{-6} Torr and 30 °C for the Al_2O_3 glass layer, respectively, during the deposition. The typical thicknesses of the four layers were 100, 300, 100, and 1000 nm, respectively. A thickness of 300 nm was selected for the BTO layer because it is reported that ferroelectric properties of BTO diminish with reduced thickness [29]. No measurements were conducted on thinner sheets. The as-grown film was then placed in pure water at 25 °C to dissolve the CaO layer, and the freestanding sheet was peeled off from the substrate.

The crystal structures of the as-grown film and sheet were evaluated using high-resolution X-ray diffraction (XRD; ATX-G, Rigaku Co., Japan) with a Cu $K\alpha_1$ radiation source. The surface morphology was studied using atomic force microscopy (AFM; Nanocute, Hitachi High-Tech Science, Japan). The ferroelectric properties of the sheets were measured using a ferroelectric tester

(Multiferroic II, Radiant Technologies, Inc., USA). The displacement was detected by a laser Doppler vibration system (VibroOne, Polytec GmbH, Germany), while the electric field was applied using the ferroelectric tester. For these measurements, freestanding BTO sheets attached to the PET substrate were used. The bottom electrode was the ITO layer, and Pt electrodes with diameters of 100 μm and 200 μm were used as the top electrodes for the ferroelectric and piezoelectric measurements.

3. Results and discussion

Figure 1 shows a schematic of the synthesis process of the freestanding oxide sheet using the CaO sacrificial layer. The as-grown film on the YSZ(110) substrate consisted of four layers: a sacrificial CaO layer, ferroelectric BTO layer, electrode ITO layer, and protective Al_2O_3 glass layer. ITO was used as the bottom electrode layer for ferroelectric and piezoelectric measurements, whereas BTO was the functional layer responsible for ferroelectricity and piezoelectricity. Al_2O_3 glass served as a protective layer for suppressing the generation of cracks. The thickness of the Al_2O_3 glass layer was set to 1000 nm, which was sufficient to obtain a crack-free millimeter-sized sheet using the SAO sacrificial layer [30]. The typical thicknesses of the four layers were 100, 300, 100, and 1000 nm, respectively.

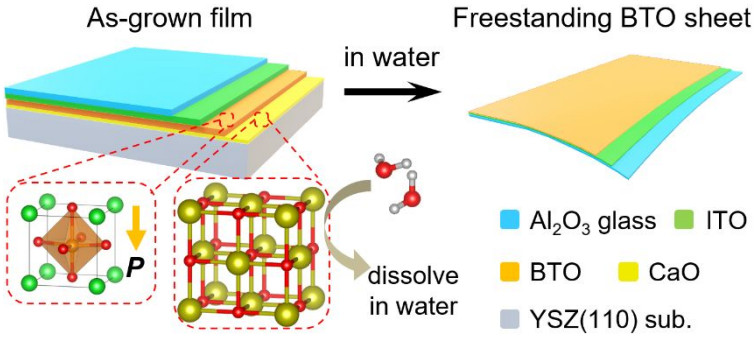

Figure 1. Schematic of the synthesis process of the freestanding BTO sheet using the CaO sacrificial layer.

Figure 2(a) shows the out-of-plane XRD pattern of the as-grown film. The 001 diffraction peak of CaO was clearly observed at $q_z/2\pi$ = 4.15 nm^{-1}, together with the 001 and 002 diffraction peaks of BTO at 2.47 and 4.94 nm^{-1}, respectively. The out-of-plane axis length of the CaO layer was 0.4820

nm, which is slightly shorter than the *a*-axis length of bulk CaO with a cubic structure (0.4881 nm) [31]. Figure 2(b) shows the reciprocal space mapping (RSM) image of the as-grown film around the 420 diffraction peak of YSZ. The 103 diffraction peak of BTO appeared at $q_x/2\pi$ = 2.49 and $q_z/2\pi$ = 7.41 nm^{-1}. Based on these results, the lattice constants of the BTO layer were estimated as a = 0.401 and c = 0.4048 nm. The c/a –1 value was 0.9 %, which is smaller than that of bulk BTO (1.2 %) [32]. Furthermore, the 103 diffraction peak of BTO extended along the q_x direction in the RSM [Fig. 2(b)]. These results may be attributed to the slight inclusion of *a*-axis-oriented domains within the predominant *c*-axis-oriented domains.

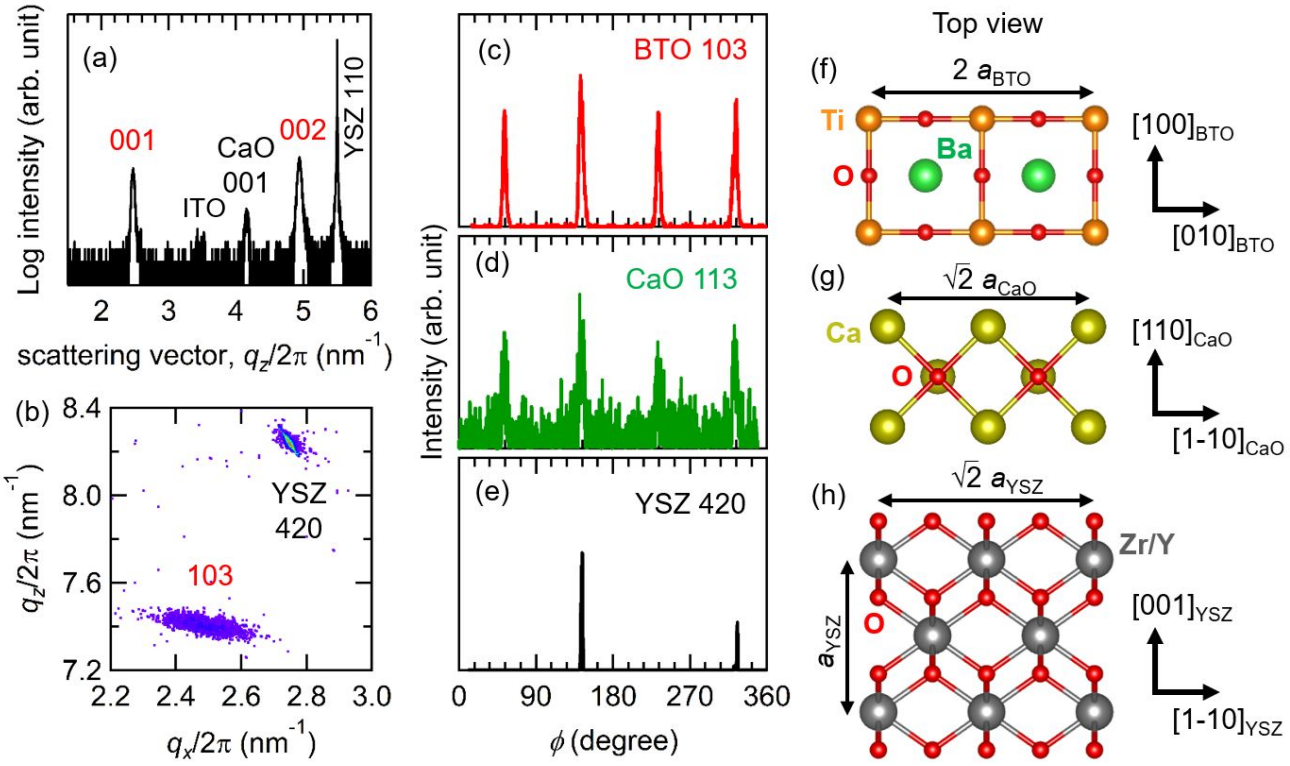

Figure 2. (a) Out-of-plane XRD pattern, (b) RSM, and ϕ-scans of the (c) BTO, (d) CaO {113}, and (e) YSZ {420} diffraction peaks of the as-grown film on the YSZ(110) substrate. Top-view images of the crystal structures of the (f) BTO and (g) CaO layers and the (h) YSZ substrate.

ϕ-scan measurements were performed to evaluate the in-plane crystal orientation of the as-grown film. Figure 2(c–e) shows the ϕ-scans of the BTO {103}, CaO {113}, and YSZ {420}

diffraction peaks. The BTO and CaO layers exhibited four-fold in-plane symmetry, corresponding to their *c*-axis-oriented tetragonal and cubic structures, respectively. In contrast, the YSZ substrate exhibited a two-fold in-plane symmetry, reflecting the [110]-orientation of its cubic structure. The ϕ values of the {103} diffraction peaks of BTO were the same as those of the {113} and {224} diffraction peaks of CaO and YSZ. These results indicate that the [100] direction of the BTO layer ($[100]_{BTO}$) is parallel to the [110] direction of the CaO layer ($[110]_{CaO}$) and the [001] and [1-10] directions of the YSZ substrate ($[001]_{YSZ}$ and $[1\text{-}10]_{YSZ}$). Furthermore, the $[001]_{BTO}$ direction was parallel to the $[001]_{CaO}$ and $[110]_{YSZ}$ directions.

Figure 2(f–h) shows top-view images of the crystal structures of the BTO and CaO layers and the YSZ substrate in the as-grown film. First, we discuss the in-plane lattice matching between the BTO and CaO layers. In this regard, we focus on the Ba–Ba distance in the BTO layer (a_{BTO} = 0.3992 nm) and the Ca–Ca distance along the $[110]_{CaO}$ direction ($\sqrt{2}/2\ a_{CaO}$ = 0.3451 nm), where a_{BTO} and a_{CaO} represent the *a*-axis lengths of bulk BTO and CaO, respectively. The Ba–Ba distance in the BTO layer was approximately 16 % longer than the Ca–Ca distance in the CaO layer. Because of this significant lattice mismatch between the CaO and BTO layers, the BTO layer is expected to grow in a relaxed manner on the CaO layer, resulting in a slight inclusion of *a*-axis-oriented domains within the predominant *c*-axis-oriented domains. However, two types of in-plane lattice matching are present between the CaO layer and YSZ substrate. The Zr–Zr distance in the YSZ substrate was 0.514 (= a_{YSZ}) and 0.727 nm (= $\sqrt{2}\ a_{YSZ}$) along the $[001]_{YSZ}$ and $[1\text{-}10]_{YSZ}$ directions, respectively. Compared to the corresponding Ca–Ca distance in the CaO layer ($3\sqrt{2}/4\ a_{CaO}$ = 0.518 and $\sqrt{2}\ a_{CaO}$ = 0.690 nm), the lattice mismatch values were 0.7 and –5 %, respectively.

The as-grown film was placed in pure water and peeled off the substrate. Figure 3(a–e) shows photographs of the as-grown film after immersing in pure water for different durations (0, 100, 200, 300, and 310 min). The thin film gradually separated from the substrate, starting at the edges, as the sacrificial CaO layer dissolved in the water. After 310 min, the CaO layer completely dissolved, allowing the freestanding BTO sheet to detach from the substrate. The sheet consists of an Al_2O_3 glass layer on the top and a BTO layer on the bottom. The bending occurs due to in-plane shrinkage of the

BTO layer after the dissolution of the sacrificial layer. Bulk BTO transitions from cubic to tetragonal as it cools below the ferroelectric transition temperature (~120°C). The BTO film was deposited above this temperature, and upon cooling, a *c*-axis-oriented film was formed. Residual strain from the substrate limits full in-plane relaxation, but after the sacrificial layer dissolves, the in-plane lattice shrinks fully, causing the sheet to bend. Figure S1 shows the AFM image of the BTO sheet, with an root mean square roughness of 4.4 nm. The dissolution rate of the 100-nm-thick CaO layer in pure water was approximately 0.24 mm/h, which is ten times slower than that of the 50-nm-thick $Sr_3Al_2O_6$ sacrificial layer (2.5 mm/h) [33]. The freestanding BTO sheet with a lateral size of 5 mm × 2 mm did not show cracks [Fig. 3(f)] owing to the crack-resistance properties of the protective Al_2O_3 glass layer. We also tested various thicknesses of the CaO layers: 30 and 70 nm. The CaO layer did not dissolve even at a thickness of 30 nm at room temperature. At 70 nm, more than one day was required to fully dissolve the CaO layer. In order to scale up to inch-scale fabrication of BTO membranes, increasing the dissolution rate of the sacrificial layer through elevated temperatures or optimizing the sacrificial layer thickness is considered important. Figure S2 shows photograph of the BTO/CaO as-grown film without the protective layer after immersion in water. Cracks and pinholes formed in the film, with pinholes spaced approximately 100 μm apart, showing the importance of the protective layer in maintaining the sheet's quality.

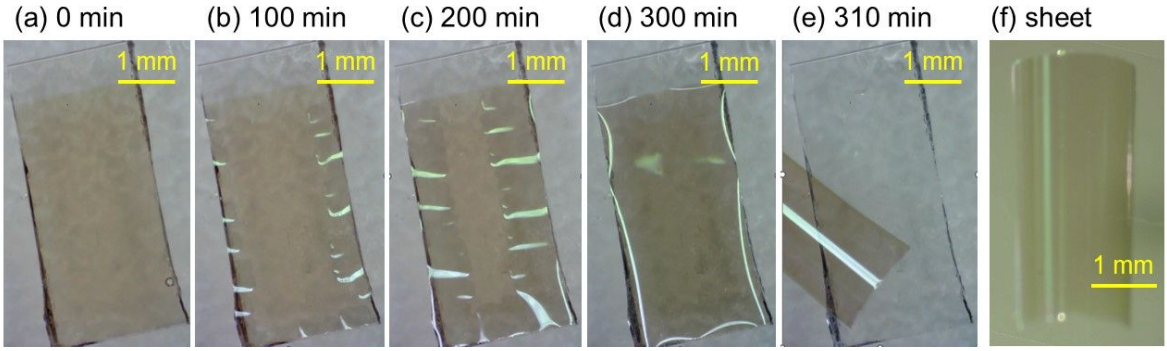

Figure 3. Photographs of the as-grown film after being placed in pure water for (a) 0, (b) 100, (c) 200, (d) 300, and (e) 310 min. (f) Photograph of the freestanding BTO sheet.

Figure 4(a) shows the out-of-plane XRD pattern of the freestanding BTO sheet. Before immersing the sample in water, an adhesive-coated PET substrate was adhered to the surface of the film. The film was then separated from the substrate along with the PET, which served as a new support substrate and flattened the shape of the film. The XRD measurements were conducted on the freestanding BTO sheets attached to the PET substrate. Its XRD pattern showed that the 001 diffraction peak of CaO disappeared, whereas the 001 and 002 diffraction peaks of BTO remained unchanged. The *c*-axis length of the BTO layer was 0.404 nm, which was almost the same as that of the as-grown film. In addition, the 103 diffraction peak of BTO was observed in the RSM image [Fig. 4(b)]. These results confirmed that the crystal orientation of the BTO layer was maintained even after the film was separated from the substrate. Figure S3 shows the rocking curve of the 002 diffraction peaks of BTO for the as-grown film and freestanding sheet; the full width at half maximum (FWHM) values were 0.92 and 1.20°, respectively.

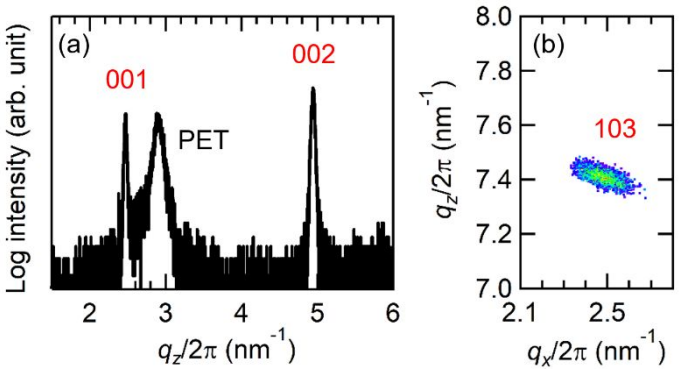

Figure 4. (a) Out-of-plane XRD pattern and (b) RSM of the BTO sheet transferred onto the PET substrate.

Figure 5(a) shows the plots of polarization and current versus the electric field (*P*–*E* and *I*–*E*) for the BTO sheet. The measurements were performed at 300 K and 10 kHz. A distinct ferroelectric hysteresis loop was observed in the *P*–*E* curve, accompanied by polarization reversal current peaks in the *I*–*E* curve, confirming the room-temperature ferroelectricity of the BTO sheet. The coercive field value of the BTO sheet is 0.5 MV/cm. The remnant polarization value was 15 μC/cm^2, which is smaller

than that of the bulk single-crystal BTO (25 μC/cm^2). This is probably due to the smaller c/a–1 value of the film (0.9 %) than that of the bulk film (1.2 %). Figure 5(b) shows the plot of displacement versus E along the out-of-plane direction of the BTO sheet. A clear butterfly curve was observed, confirming the piezoelectricity of the BTO sheet. The d_{33} value was 270 pm/V, which is higher than those obtained for epitaxial films grown on substrates, and approaches the piezoelectric coefficient of domain-engineered bulk BTO [35,36]. In epitaxial films, the piezoelectric strain is suppressed owing to the substrate-clamping effect. However, after the film was separated from the substrate, its state approached that of single crystals, resulting in enhanced piezoelectric properties [36]. The d_{33} value reported in this study was measured using a laser Doppler vibration system. However, it is important to note that this method may be influenced by artifacts, such as distortion of substrates. Accurate evaluation requires simultaneous measurements from both the front and back sides of the substrate to account for these artifacts. Since this study only performed top-side measurements, the reported d_{33} value may be overestimated. Further investigations are needed to validate these findings.

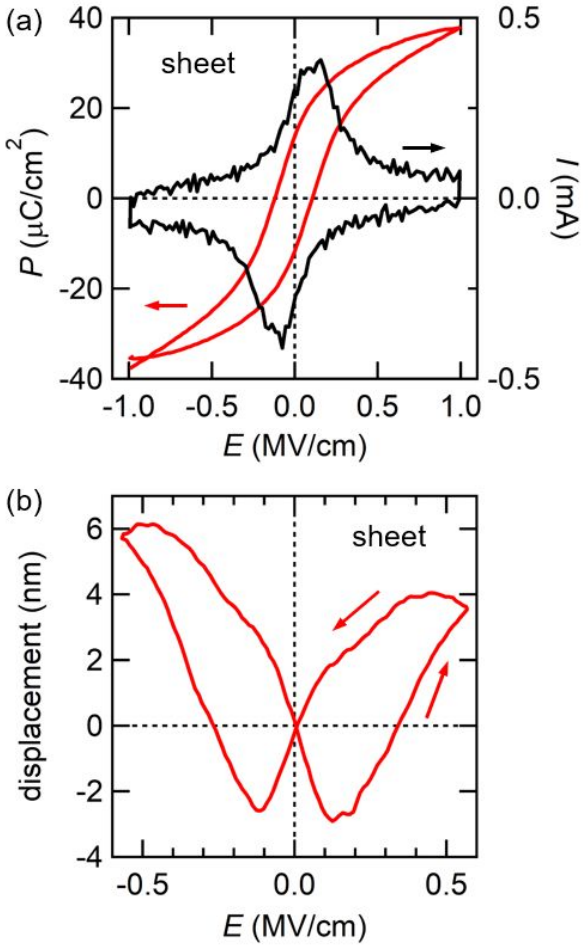

Figure 5. (a) Plots of polarization (*P*), current (*I*), and (b) displacement versus the electric field (*E*) for the BTO sheet at 10 kHz and 300 K. The thickness of the BTO layer was 300 nm

Further, we investigated the reusability of the YSZ substrate. After peeling the film from the YSZ substrate, ultrasonic cleaning was performed in pure water for 5 min to remove any residual material from the surface. The substrate was then reused to fabricate a new film [Fig. 6(a)]. Figure 6(b) shows the surface morphology of the YSZ substrate after the ultrasonic cleaning. The root mean square of the roughness of the YSZ substrate was 0.16 nm, which is close to that of the new substrate (Figure S4). Figure 6(c) shows out-of-plane XRD patterns of the as-grown films and sheets after the first and second cycles. In the XRD profiles of all the samples, the 002 diffraction peaks of BTO were clearly observed. The XRD results indicated no significant differences between the first and second cycles, demonstrating that the substrate could be effectively reused.

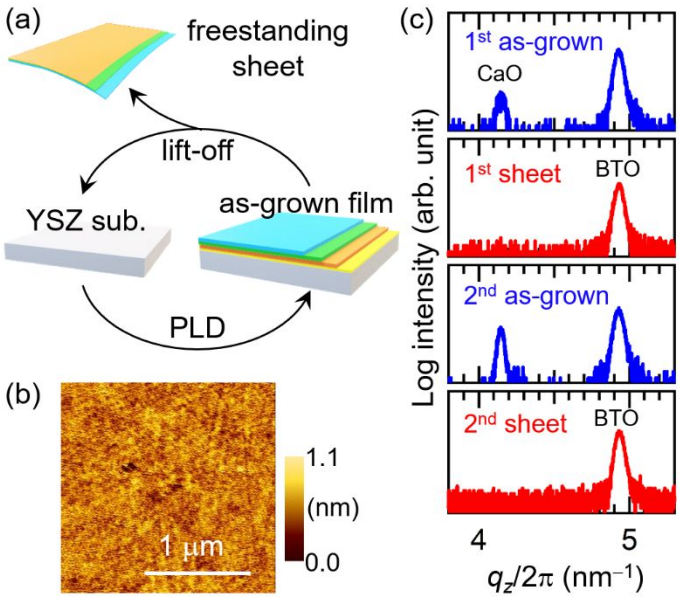

Figure 6. (a) Schematic of the reusability process of the YSZ substrate. (b) Surface morphology of the YSZ substrate after the first cycle. (c) Out-of-plane XRD patterns of the as-grown films and sheets after the first and second cycles.

Conclusion

In this study, we demonstrated the synthesis of a crack-free, freestanding BTO epitaxial sheet using a CaO sacrificial layer grown on a YSZ(110) substrate. The BTO film was successfully peeled from the substrate by dissolving the CaO sacrificial layer in pure water, resulting in a high-quality epitaxial sheet with a lateral size of 5 mm × 2 mm. The freestanding BTO sheet exhibited excellent room-temperature ferroelectric and piezoelectric properties, with a d_{33} value of 270 pm/V, which was higher than those of epitaxial films grown on substrates because of the relaxation of the substrate-induced strain. Furthermore, the reusability of the YSZ substrate enhances the practicability of this method for industrial applications. This study broadens the potential for integrating freestanding ferroelectric oxide sheets into flexible electronics and other advanced technologies.

Supporting Information

Details of XRD and AFM results are provided in the Supporting Information.

Acknowledgments

This work was supported by JST, PRESTO, Grant Number JPMJPR21Q3 (T.K.). W. Z. was supported by the JST SPRING (grant number: JPMJSP2119).

References

[1] Choi, K. J.; Biegalski, M.; Li, Y.; Sharan, A.; Schubert, J.; Uecker, R.; Reiche, P.; Chen, Y.; Pan, X.; Gopalan, V. Enhancement of ferroelectricity in strained $BaTiO_3$ thin films. Science 2004, 306, 1005-1009.

[2] Shrout, T. R.; Zhang, S. J. Lead-free piezoelectric ceramics: Alternatives for PZT. J. Electroceramics 2007, 19, 113-126.

[3] Li, J.; Li, F.; Xu, Z.; Zhang, S. Multilayer lead-free ceramic capacitors with ultrahigh energy density and efficiency. Adv. Mater. 2018, 30, 1802155.

[4] Boes, A.; Chang, L.; Langrock, C.; Yu, M.; Zhang, M.; Lin, Q.; Lončar, M.; Fejer, M.; Bowers, J.; Mitchell, A. Lithium niobate photonics: Unlocking the electromagnetic spectrum. Science 2023, 379, 40.

[5] Wei, D.; Wang, C.; Wang, H.; Hu, X.; Wei, D.; Fang, X.; Zhang, Y.; Wu, D.; Hu, Y.; Li, J. Experimental demonstration of a three-dimensional lithium niobate nonlinear photonic crystal. Nat. Photo. 2018, 12, 596-600.

[6] He, Y.; Yang, Q.-F.; Ling, J.; Luo, R.; Liang, H.; Li, M.; Shen, B.; Wang, H.; Vahala, K.; Lin, Q. Self-starting bi-chromatic $LiNbO_3$ soliton microcomb. Optica 2019, 6, 1138-1144.

[7] Lu, D.; Baek, D. J.; Hong, S. S.; Kourkoutis, L. F.; Hikita, Y.; Hwang, H. Y. Synthesis of freestanding single-crystal perovskite films and heterostructures by etching of sacrificial water-soluble layers. Nat. Mater. 2016, 15, 1255-1260.

[8] Ji, D.; Cai, S.; Paudel, T. R.; Sun, H.; Zhang, C.; Han, L.; Wei, Y.; Zang, Y.; Gu, M.; Zhang, Y. Freestanding crystalline oxide perovskites down to the monolayer limit. Nature 2019, 570, 87-90.

[9] Han, L.; Addiego, C.; Prokhorenko, S.; Wang, M.; Fu, H.; Nahas, Y.; Yan, X.; Cai, S.; Wei, T.; Fang, Y. High-density switchable skyrmion-like polar nanodomains integrated on silicon. Nature 2022, 603, 63-67.

[10] Dong, G.; Li, S.; Yao, M.; Zhou, Z.; Zhang, Y.-Q.; Han, X.; Luo, Z.; Yao, J.; Peng, B.; Hu, Z. Super-elastic ferroelectric single-crystal membrane with continuous electric dipole rotation. Science 2019, 366, 475-479.

[11] Gu, K.; Katayama, T.; Yasui, S.; Chikamatsu, A.; Yasuhara, S.; Itoh, M.; Hasegawa, T. Simple method to obtain large-size single-crystalline oxide sheets. Adv. Funct. Mater. 2020, 30, 2001236.

[12] Yang, A. J.; Han, K.; Huang, K.; Ye, C.; Wen, W.; Zhu, R.; Zhu, R.; Xu, J.; Yu, T.; Gao, P. Van der Waals integration of high-κ perovskite oxides and two-dimensional semiconductors. Nat. Electron. 2022, 5, 233-240.

[13] Huang, J.-K.; Wan, Y.; Shi, J.; Zhang, J.; Wang, Z.; Wang, W.; Yang, N.; Liu, Y.; Lin, C.-H.; Guan, X. High-κ perovskite membranes as insulators for two-dimensional transistors. Nature 2022, 605, 262-267.

[14] Gong, L.; Yu, R.; Ohta, H.; Katayama, T. Synthesis and transparent conductivity of crack-free La:$BaSnO_3$ epitaxial flexible sheets. Dalton transactions 2023, 52, 6317-6323.

[15] Yu, R.; Gong, L.; Ohta, H.; Katayama, T. Ferroelectricity, High Permittivity, and Tunability in Millimeter-Size Crack-Free $Ba_{1-x}Sr_xTiO_3$ Flexible Epitaxial Sheets. ACS Appl. Electron. Mater. 2023, 5, 5234-5239.

[16] L. Gong, A. T., W. Zhou, R. Mitsuya, H.; Ohta, T. K. Ferroelectric $BaTiO_3$ Freestanding Sheets for Ultra-High-Speed Light-Driven Actuator. ACS Appl. Mater. Interfaces 2024, 16, 54146–54153.

[17] Hong, S. S.; Gu, M.; Verma, M.; Harbola, V.; Wang, B. Y.; Lu, D.; Vailionis, A.; Hikita, Y.; Pentcheva, R.; Rondinelli, J. M. Extreme tensile strain states in $La_{0.7}Ca_{0.3}MnO_3$ membranes. Science 2020, 368, 71-76.

[18] Singh, P.; Swartz, A.; Lu, D.; Hong, S. S.; Lee, K.; Marshall, A. F.; Nishio, K.; Hikita, Y.; Hwang,

H. Y. Large-area crystalline $BaSnO_3$ membranes with high electron mobilities. ACS Appl. Electron. Mater. 2019, 1, 1269-1274.

[19] Bakaul, S. R.; Serrao, C. R.; Lee, M.; Yeung, C. W.; Sarker, A.; Hsu, S.-L.; Yadav, A. K.; Dedon, L.; You, L.; Khan, A. I. Single crystal functional oxides on silicon. Nature commun. 2016, 7, 10547.

[20] Bourlier, Y.; Bérini, B.; Frégnaux, M.; Fouchet, A.; Aureau, D.; Dumont, Y. Transfer of epitaxial $SrTiO_3$ nanothick layers using water-soluble sacrificial perovskite oxides. ACS Appl. Mater. Interfaces 2020, 12, 8466-8474.

[21] Pesquera, D.; Khestanova, E.; Ghidini, M.; Zhang, S.; Rooney, A. P.; Maccherozzi, F.; Riego, P.; Farokhipoor, S.; Kim, J.; Moya, X. Large magnetoelectric coupling in multiferroic oxide heterostructures assembled via epitaxial lift-off. Nat. Commun. 2020, 11, 3190.

[22] Peng, H.; Lu, N.; Yang, S.; Lyu, Y.; Liu, Z.; Bu, Y.; Shen, S.; Li, M.; Li, Z.; Gao, L. A Generic Sacrificial Layer for Wide-Range Freestanding Oxides with Modulated Magnetic Anisotropy. Adv. Funct. Mater. 2022, 32, 2111907.

[23] Chang, Y.W.; Wu, P.C.; Yi, J.B.; Liu, Y.C.; Chou, Y.; Chou, Y.C.; Yang, J.C. A fast route towards freestanding single-crystalline oxide thin films by using $YBa_2Cu_3O_{7-x}$ as a sacrificial layer. Nanoscale Research Lett. 2020, 15, 1-8.

[24] Varshney, S.; Choo, S.; Thompson, L.; Yang, Z.; Shah, J.; Wen, J.; Koester, S. J.; Mkhoyan, K. A.; McLeod, A. S.; Jalan, B. Hybrid Molecular Beam Epitaxy for Single-Crystalline Oxide Membranes with Binary Oxide Sacrificial Layers. ACS Nano 2024, 18, 6348-6358.

[25] Takahashi, R.; Lippmaa, M. Sacrificial water-soluble BaO layer for fabricating free-standing piezoelectric membranes. ACS Appl. Mater. Interfaces 2020, 12, 25042-25049.

[26] Guo, R.; You, L.; Lin, W.; Abdelsamie, A.; Shu, X.; Zhou, G.; Chen, S.; Liu, L.; Yan, X.; Wang, J. Continuously controllable photoconductance in freestanding $BiFeO_3$ by the macroscopic flexoelectric effect. Nat. Commun. 2020, 11, 2571.

[27] Borik, M.; Lomonova, E.; Osiko, V.; Panov, V.; Porodinkov, O.; Vishnyakova, M.; Voron'ko, Y. K.; Voronov, V. Partially stabilized zirconia single crystals: growth from the melt and

investigation of the properties. Journal of Crystal Growth 2005, 275, e2173-e2179.

[28] Tateno, Y.; Endo, K.; Arisawa, S.; Vlaicu, A.-M.; Nedelcu, L.; Preda, N.; Secu, M.; Iordanescu, R.; Kuncser, A. C.; Badica, P. Growth of SrTiO3 single crystals with a diameter of about 30 mm by the Verneuil method. Crystal Growth & Design 2018, 19, 604-612.

[29] Huang,G F, Berger, S. Combined effect of thickness and stress on ferroelectric behavior of thin $BaTiO_3$ films. J. Appl. Phys. 2003, 93: 2855-2860.

[30] Gong, L.; Wei, M.; Yu, R.; Ohta, H.; Katayama, T. Significant Suppression of Cracks in Freestanding Perovskite Oxide Flexible Sheets Using a Capping Oxide Layer. ACS Nano 2022, 16, 21013-21019.

[31] Fiquet, G.; Richet, P.; Montagnac, G. High-temperature thermal expansion of lime, periclase, corundum and spinel. Phys. Chem. Minerals 1999, 27, 103-111.

[32] Kwei, G.; Lawson, A.; Billinge, S.; Cheong, S. Structures of the ferroelectric phases of barium titanate. J. Phys. Chem. 1993, 97, 2368-2377.

[33] Nian, L.; Sun, H.; Wang, Z.; Xu, D.; Hao, B.; Yan, S.; Li, Y.; Zhou, J.; Deng, Y.; Hao, Y. $Sr_4Al_2O_7$: A new sacrificial layer with high water dissolution rate for the synthesis of freestanding oxide membranes. Adv. Mater. 2024, 36, 2307682.

[34] Wada, S.; Yako, K.; Kakemoto, H.; Tsurumi, T.; Kiguchi, T. Enhanced piezoelectric properties of barium titanate single crystals with different engineered-domain sizes. J. Appl. Phys. 2005, 98, 014109 .

[35] Kelley, K.; Yilmaz, D.; Collins, L.; Sharma, Y.; Lee, H.; Akbarian, D.; Van Duin, A.; Ganesh, P.; Vasudevan, R. Thickness and strain dependence of piezoelectric coefficient in $BaTiO_3$ thin films. Phys. Rev. Mater. 2020, 4, 024407.

[36] Lindemann, S.; Irwin, J.; Kim, G. Y.; Wang, B.; Eom, K.; Wang, J.; Hu, J.; Chen, L. Q.; Choi, S. Y.; Eom, C. B. Low-voltage magnetoelectric coupling in membrane heterostructures. Sci. Adv. 2021, 7, eabh2294.

Data availability statements

The data supporting this article have been included as part of the Supplementary Information.